



# Improved performance of Zn-doped SnO<sub>2</sub> modified g-C<sub>3</sub>N<sub>4</sub> for visible light-driven photocatalysis

Wei Liu<sup>1,2</sup> · Qun Kang<sup>1,2</sup> · Ling Wang<sup>1,2</sup> · Lilian Wen<sup>1,2</sup> · Zhaohua Li<sup>1,2</sup>

Received: 27 July 2021 / Accepted: 2 March 2022 / Published online: 7 March 2022  
© The Author(s), under exclusive licence to Springer-Verlag GmbH Germany, part of Springer Nature 2022

## Abstract

The low-cost composite of g-C<sub>3</sub>N<sub>4</sub> modified by Zn-doped SnO<sub>2</sub> nanoparticles was prepared for the first time in this work. The characterization results of XRD and SEM demonstrated that Zn was successfully doped into SnO<sub>2</sub>. The formed Sn-O-Zn bonds and interaction between the Zn-doped SnO<sub>2</sub> sample and g-C<sub>3</sub>N<sub>4</sub> in the composite were explored by FT-IR and XPS technologies. Photocatalytic degradation experiments showed that the as-prepared optimal composite photocatalyst displayed enhanced photocatalytic reactivity towards both dyes and antibiotics, which could degrade 85.6% of RhB and 86.8% of tetracycline within 30 and 90 min, respectively. The oxygen vacancies formed in SnO<sub>2</sub> after Zn doping could capture the photogenerated electrons of g-C<sub>3</sub>N<sub>4</sub>, thereby promoting the separation of photogenerated electron-hole pairs, then more ·O<sub>2</sub><sup>-</sup> and holes can be generated during the visible light-driven photocatalytic reaction, so that the composite of Zn-doped SnO<sub>2</sub>/g-C<sub>3</sub>N<sub>4</sub> acquired higher photocatalytic activity and accelerated the degradation of target organics. Active species capturing experiments and ESR detection results also confirmed that ·O<sub>2</sub><sup>-</sup> and holes were the main active species in the reaction process. This work developed a novel g-C<sub>3</sub>N<sub>4</sub>-based photocatalyst with no noble metal, low price, and high photocatalytic activity, which could provide a cost-effective and high-efficiency strategy for wastewater treatment.

**Keywords** Zn-doped SnO<sub>2</sub> · g-C<sub>3</sub>N<sub>4</sub> · Composite photocatalyst · Photocatalytic degradation · Visible light irradiation

## Introduction

The problem of organic pollution is a negative impact on the environment caused by the rapid development of modern industry, which is extremely unfavorable to the sustainable development of the environment and human health. Therefore, exploring and developing efficient elimination approaches for organic pollutants is the priority (Xue et al., 2019). Semiconductor-based photocatalysis overcomes the disadvantages of insufficient degradation efficiency faced by traditional pollutant removal technologies such as adsorption and filtration which have been getting increasing attention (Balu et al., 2020). For photocatalysis, active free radicals

will be generated depending on the conversion of photon energy by the photocatalyst, and the attack behavior of active free radicals on the structure of organic matter is the key and efficient way to decompose the targets.

Benefit from the characteristics of photocatalysis that converts light energy into chemical energy, it is considered a green and clean solar energy conversion technology, which has been widely applied in solving the current serious problems ranging from environmental pollution to energy shortage (Ismael, 2020). Recently, researches on photocatalysts have mainly focused on semiconductors that respond to visible light. Visible light-driven photocatalysts will undoubtedly expand the utilization of solar energy, thereby enhancing the photocatalytic activity of the photocatalyst at a high level. Among them, a polymeric semiconductor material, graphitic carbon nitride (g-C<sub>3</sub>N<sub>4</sub>) with intermediate band-gap (2.7 eV), has become the most famous photocatalyst in recent years.

g-C<sub>3</sub>N<sub>4</sub> can be simply prepared by high-temperature condensation polymerization by melamine, dicyandiamide, and urea as the precursor material (Chen et al., 2020; Rattan Paul and Nehra, 2021). The unique and

Responsible Editor: Sami Rtimi

✉ Qun Kang  
kangq\_hubu@126.com

<sup>1</sup> Faculty of Resources and Environmental Science, Hubei University, Wuhan 430062, China

<sup>2</sup> Hubei Engineering Research Center for Rural Drinking Water Safety, Wuhan 430062, China

attractive characteristics of g-C<sub>3</sub>N<sub>4</sub> including the simple reaction operation, the flexible two-dimensional (2D) layered structure, and the high thermal and chemical stability enable it to be extensively researched and applied in different fields such as contaminants degradation (Amedlous et al., 2021; Wang et al., 2020), sterilization (Ding et al., 2020), nitrogen fixation (Li et al., 2021), CO<sub>2</sub> and NO conversion (Guo et al., 2021; Liu et al., 2021a), and energy production (Feng et al., 2021; Wang et al., 2021a). However, the structural defects in g-C<sub>3</sub>N<sub>4</sub> would easily lead to the rapid recombination of photogenerated carriers, which greatly inhibits its photocatalytic activity. This will hinder the path of g-C<sub>3</sub>N<sub>4</sub> from laboratory research to practical application. Many studies reported that the usage of introducing metallic (Paul et al., 2020b) or non-metallic elements (Chu et al., 2020) into the structure of g-C<sub>3</sub>N<sub>4</sub>, or the formation of heterojunctions by combining g-C<sub>3</sub>N<sub>4</sub> with other semiconductor photocatalysts such as TiO<sub>2</sub> (Sun et al., 2019), SiO<sub>2</sub> (Sun et al., 2021), ZnO (Paul et al., 2020a), and Bi<sub>2</sub>MoO<sub>6</sub> (Liu et al., 2021), can effectively enhance the photocatalytic activity of g-C<sub>3</sub>N<sub>4</sub>. Combination with semiconductors could improve the interface structure and promote the separation of photogenerated carriers in g-C<sub>3</sub>N<sub>4</sub>, which is an effective strategy employed to enhance the photocatalytic activity of g-C<sub>3</sub>N<sub>4</sub> (Li et al., 2020).

Among various diversified semiconductors, the low-cost SnO<sub>2</sub> with a bandgap of about 3.6 eV has received great attention owing to its non-toxicity, chemical stability, and electrical conductivity. SnO<sub>2</sub> has mostly been used for the preparation of gas sensors (Phuoc et al., 2020), solar cells (Huang et al., 2020), photocatalyst (Liu et al., 2021b; Yakout, 2021), etc. While the large bandgap of SnO<sub>2</sub> limits the utilization of solar energy, it is unreachable for it to perform photocatalytic application under visible light. As a useful improvement measure, doping metal ions such as Ga (Sivakumar et al., 2021), Nd (Song et al., 2021), Ce (Pacheco-Salazar et al., 2020), Ni, and Co (Matussin et al., 2020) into SnO<sub>2</sub> is an important means. The conductivity and optical absorption of SnO<sub>2</sub> can be improved by metal doping. Moreover, the surface activity of SnO<sub>2</sub> can get enhanced, thereby the better performance of it can be acquired.

Some literature reported that when Zn was incorporated into SnO, the microstructure and the defect chemistry of the SnO<sub>2</sub> could be modified (Ma and Wei, 2018; Wu et al., 2021). On account of the similar ion radius of Zn<sup>2+</sup> and Sn<sup>4+</sup> (0.074 nm for Zn<sup>2+</sup>, 0.071 nm for Sn<sup>4+</sup>), the introduction of Zn will cause the generation of oxygen vacancies for charge compensation while maintaining the integrity of SnO<sub>2</sub> lattice (Zhao et al., 2015). It also has the advantage of increasing adsorption sites, which is beneficial for photocatalysis (Adhikari et al., 2018). Therefore, the introduction of Zn-doped SnO<sub>2</sub> into g-C<sub>3</sub>N<sub>4</sub> is expected to improve the

separation efficiency of photogenerated carriers of g-C<sub>3</sub>N<sub>4</sub>, which can contribute to the improvement of the photocatalytic activity of the photocatalyst.

To date, there are rare works that have been reported about the Zn-doped SnO<sub>2</sub>/g-C<sub>3</sub>N<sub>4</sub> composites and their photocatalytic performances. Therefore, the combination of Zn-doped SnO<sub>2</sub> nanoparticles with g-C<sub>3</sub>N<sub>4</sub> proposed here is an innovative work, which utilizes the oxygen vacancies generated by Zn-doped SnO<sub>2</sub> to capture the photogenerated electrons of g-C<sub>3</sub>N<sub>4</sub>, and promotes the separation of photogenerated carriers of g-C<sub>3</sub>N<sub>4</sub>, finally improving the degradation efficiency of dyes and antibiotic contaminants represented by Rhodamine B (RhB) and tetracycline (TC). By combining the characterization results of the physicochemical properties of the as-prepared photocatalysts and the evaluation analysis of their photocatalytic activities, we revealed the mechanism of the Zn-doped SnO<sub>2</sub>/g-C<sub>3</sub>N<sub>4</sub> composite photocatalyst with enhanced visible light-driven photocatalytic activity for contaminant degradation. Moreover, this work synthesized a photocatalyst with no noble metal, low price, and high photocatalytic activity, which could provide a cost-effective and high-efficiency strategy for wastewater treatment.

## Material and methods

### Materials

All the chemicals used in the work were of analytical grade.

The chemicals required for the material preparation process (including urea, Tin chloride pentahydrate (SnCl<sub>4</sub>·5H<sub>2</sub>O), zinc acetate dihydrate (Zn(CH<sub>3</sub>COO)<sub>2</sub>·2H<sub>2</sub>O), NH<sub>3</sub>·H<sub>2</sub>O, and absolute ethyl alcohol) and the target pollutants of RhB were all purchased from Sinopharm Chemical Reagent Co., Ltd. (Shanghai, China). Tetracycline hydrochloride was purchased from Shanghai Meryer Chemical Technology Co., Ltd. (Shanghai, China).

### Preparation of g-C<sub>3</sub>N<sub>4</sub>

g-C<sub>3</sub>N<sub>4</sub> was fabricated by thermal condensation reaction. The product was obtained by heating urea to 530 °C for 2 h. After cooling, the light yellow product was placed in a mortar and ground to a fine powder to obtain the g-C<sub>3</sub>N<sub>4</sub> sample.

### Preparation of SnO<sub>2</sub> and Zn-doped SnO<sub>2</sub> materials

Hydrothermal synthesis was used to prepare SnO<sub>2</sub> and Zn-doped SnO<sub>2</sub>. Twelve millimoles of SnCl<sub>4</sub>·5H<sub>2</sub>O was dissolved in 50 mL solution containing NH<sub>3</sub>·H<sub>2</sub>O and deionized (DI) water (NH<sub>3</sub>·H<sub>2</sub>O: DI water = 1:1, v/v), and then different amounts of Zn(CH<sub>3</sub>COO)<sub>2</sub>·2H<sub>2</sub>O (0, 0.12, 0.24,

0.36 mmol) were added into the above mixture respectively by vigorous stirring for 2 h. Then the different mixture was transferred into 100 mL Teflon-lined autoclaves and reacted at 180 °C for 12 h. When the autoclaves were cooled to room temperature, the white products were collected at the bottom by centrifugation and washed with DI water and ethanol repeatedly. After drying them at 80 °C overnight, Zn-doped SnO<sub>2</sub> samples with a different molar ratio of Zn and Sn were obtained. And we abbreviated them as SnO<sub>2</sub>, 1% ZS, 2% ZS, and 3% ZS, respectively.

### Preparation of SnO<sub>2</sub>/g-C<sub>3</sub>N<sub>4</sub> and Zn-doped SnO<sub>2</sub>/g-C<sub>3</sub>N<sub>4</sub> composites

Solvent mixing followed by the co-calcination method was selected for the synthesis of SnO<sub>2</sub>/g-C<sub>3</sub>N<sub>4</sub> and Zn-doped SnO<sub>2</sub>/g-C<sub>3</sub>N<sub>4</sub>. Specifically, put g-C<sub>3</sub>N<sub>4</sub> (0.2 g) and different amounts of 2% ZS sample (0.01, 0.03, and 0.05 g) into 10 mL solution of absolute ethyl alcohol and DI water (1:1, v/v), and then use a magnetic stirring device to continuously stir the above suspension for 2 h. Next, the above-mixed solution was placed in an oven and dried at 80 °C for 12 h. Finally, the mixed dry samples were calcined in a muffle furnace for 2 h at 400 °C to obtain 2% ZS/g-C<sub>3</sub>N<sub>4</sub> composites in mass ratios. The composites were designated as 2% ZS/CN-5, 2% ZS/CN-15, and 2% ZS/CN-25, respectively. SnO<sub>2</sub>/CN-15, 1% ZS/CN-15, and 3% ZS/CN-15 samples were prepared by using the same method.

### Characterization

The crystal phases of the as-prepared catalysts were analyzed by X-ray diffractometer (XRD, RU-200B/D/MAX-RB, Japan). The morphologies and structures of the samples were examined by field emission scanning electron microscope (FESEM, Zeiss Ultra Plus, Germany) and field emission high-resolution transmission electron microscope (FHTEM, JEM-2100F, Japan). Fourier transform infrared (FTIR) spectra of the samples were acquired on an FTIR instrument (Nicolet 6700, USA) in the range of 400–4000 cm<sup>-1</sup>. UV-vis absorption spectra of the samples were examined by a UV-vis spectrophotometer (PerkinElmer Lambda 750 S, USA). The X-ray photoelectron spectroscopy (XPS, Thermo ESCALAB 250 Xi, USA) was performed for analysis of elemental composition and valence states. Photoluminescence (PL) spectra of the materials were acquired by a fluorescence spectrophotometer (Gangdong F-380, China) equipped with a 300W Xe arc lamp at the excitation wavelength of 325 nm. The active free radicals were measured by an ESR spectrometer (Bruker A300, Germany).

### Evaluation of photocatalytic activity

The photocatalytic performance of the as-prepared g-C<sub>3</sub>N<sub>4</sub>, 2% ZS, SnO<sub>2</sub>/CN-15, 1% ZS/CN-15, 2% ZS/CN-15, and 3% ZS/CN-15 composites was evaluated by using RhB and TC as the model organic contaminants. For the degradation of RhB, 20 mg of as-prepared material was added into 100 mL RhB aqueous solution (10 mg/L), and for the degradation of TC, 50 mg photocatalyst was added into 100 mL TC aqueous solution with the concentration of 30 mg/L. Then the formed RhB (or TC) suspension was stirred in the dark circumstances for 30 min to establish an adsorption/desorption equilibrium. After that, the photodegradation was performed under visible light irradiation by using a 150 W Xe lamp with a 420-nm cut-off filter. During the photocatalytic process, 3 mL of sample solution was taken out every 5 min for RhB (10 min for TC solution), and it was filtered through a filter membrane (0.22 μm, Jinteng, China) to obtain a clear solution. Finally, the concentration of RhB (or TC) in the sample was determined by Shimadzu UV-vis spectrophotometer (mini 1240, Japan) at 554 nm (or 357 nm). The degradation efficiency is defined as  $C/C_0$ , where  $C_0$  is the concentration of the RhB (or TC) solution when photodegradation starts, and  $C$  is the concentration of the RhB (or TC) at different irradiation times.

## Results and discussion

### XRD analysis

XRD was utilized to acquire the crystal phase information of the as-prepared samples. The XRD patterns of SnO<sub>2</sub>, 1% ZS, 2% ZS, and 3% ZS are shown in Fig. 1a. The diffraction peaks at 26.6°, 33.9°, 39.0°, 51.8°, and 54.8° of these samples can be assigned to (110), (101), (200), (211), and (220) facets of the rutile SnO<sub>2</sub> (JCPDS No. 41-1445), which acted as the host material. It can be found that, when the concentration of the doped Zn<sup>2+</sup> increased from 1 to 3%, the diffraction peaks of Zn-doped SnO<sub>2</sub> shifted 0.1° towards a lower diffraction angle compared with undoped SnO<sub>2</sub>. This indicates that the doping of Zn affects the lattice parameters of SnO<sub>2</sub> (Soltan et al., 2017). Fig. 1b shows the XRD patterns of g-C<sub>3</sub>N<sub>4</sub> and 2% ZS/CN composites, and the diffraction peaks located at 12.9° and 27.6° in these samples accord with the (100) and (002) planes of g-C<sub>3</sub>N<sub>4</sub> (Liu et al., 2021c; Paul et al., 2019a). The characteristic diffraction peaks of SnO<sub>2</sub> also can be observed in the 2% ZS/CN composite, and their intensity gradually increases when the content of 2% ZS increases in the composite.

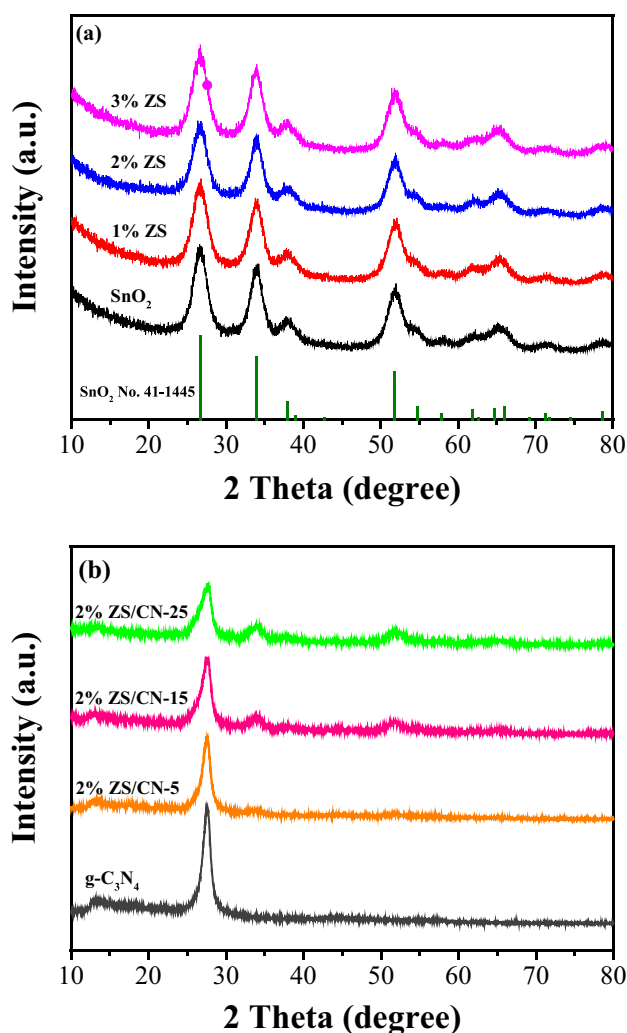


**Fig. 1** XRD patterns of SnO<sub>2</sub>, 1% ZS, 2% ZS, and 3% ZS (a) and XRD patterns of g-C<sub>3</sub>N<sub>4</sub>, 2% ZS/CN-5, 2% ZS/CN-15, and 2% ZS/CN-25 (b)

### Morphological characteristics

SEM was conducted to determine the microstructure and morphologies of g-C<sub>3</sub>N<sub>4</sub>, SnO<sub>2</sub>, 2% ZS, and 2% ZS/CN-15 samples, and Fig. 2 shows their SEM images. The slightly curled multiple nanosheet structures exhibited in Fig. 2a are a characteristic structure of 2D polymerized g-C<sub>3</sub>N<sub>4</sub> prepared by urea. Fig. 2b displays nanoparticle morphologies of the as-prepared 2% ZS, and the diameter of it ranged from 200 to 400 nm. The structure image of the composite of 2% ZS/CN-15 composite (Fig. 2c) was almost identical with the morphology of g-C<sub>3</sub>N<sub>4</sub>, owing to the small size and low content. The surface element distribution detection of the 2% ZS/CN-15 composite sample (Fig. 2c) was executed by EDS. We can observe that all the elements of C, N, O, Sn, and Zn exist in the 2% ZS/CN-15 sample, which is shown in Fig. 2d, Fig. 2e, Fig. 2f, Fig. 2g, and Fig. 2h, respectively.

The structures of g-C<sub>3</sub>N<sub>4</sub> and the 2% ZS/CN-15 composite were further identified by employing TEM (Fig. 3). As shown in Fig. 3a, g-C<sub>3</sub>N<sub>4</sub> displays a stretchable, thin, and malleable structure similar to that of graphite. Different from SEM image, the TEM of 2% ZS/CN-15 sample listed in Fig. 3b exhibits the morphology that 2% ZS nanoparticles are evenly dispersive and wrapped by g-C<sub>3</sub>N<sub>4</sub>. Moreover, we can also find out from Fig. 3c that the 2% ZS nanoparticles are aggregated by very small nanoparticles with a diameter of about 5 nm. The HR-TEM image of the 2% ZS sample shown in Fig. 3d uncovers the lattice fringes corresponding to the (110) and (101) facets of SnO<sub>2</sub> crystal, with the interplanar spacing of 0.33 nm and 0.26 nm, respectively. The visualized SEM and EDS mapping as well as TEM images not only assist in the analysis of the structure of the samples but also verify the successful synthesis of the material.

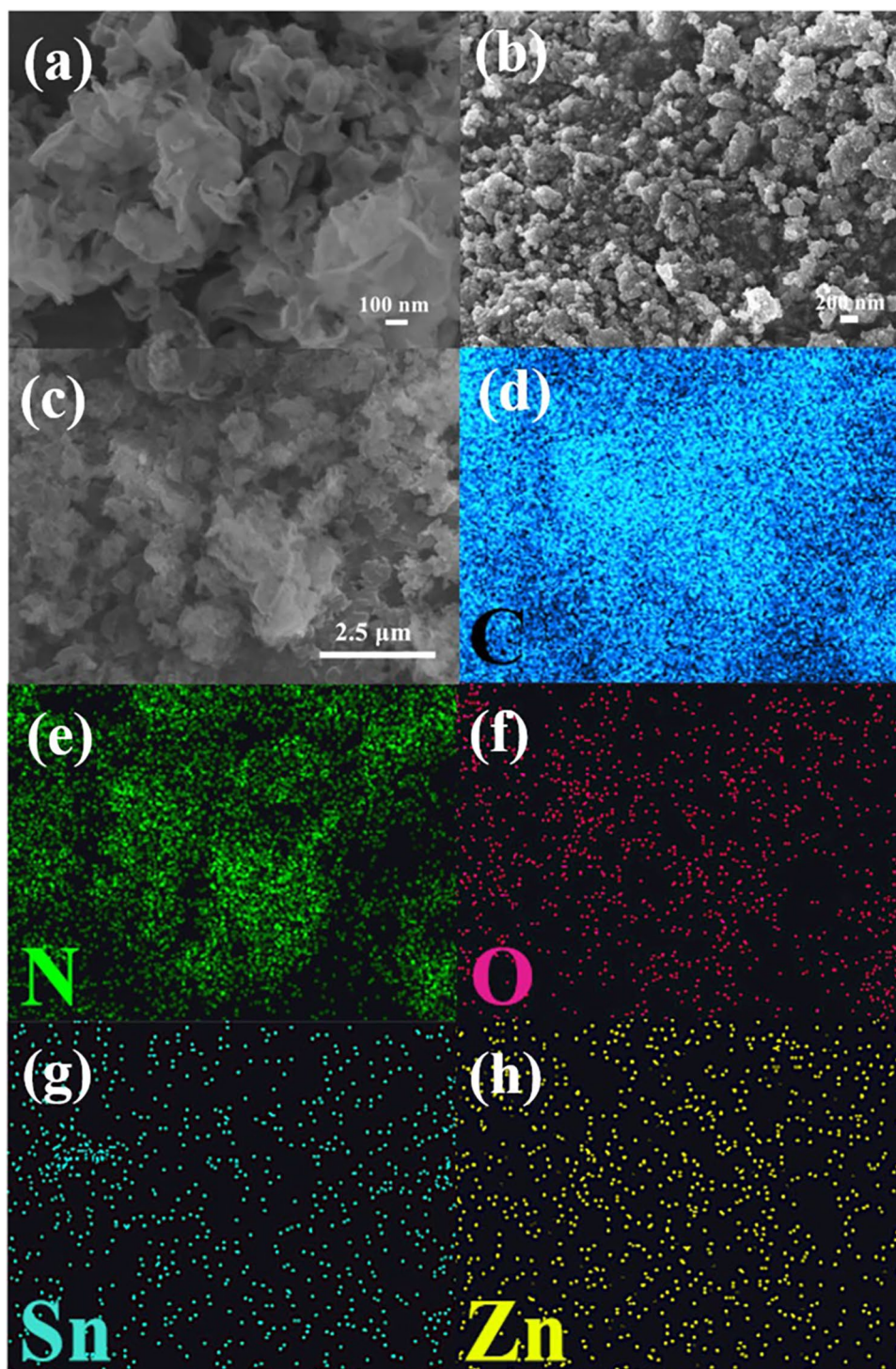
### XPS measurement

Relying on the determination of XPS, the surface components and the chemical element valence information of the materials were further investigated. Fig. 4 shows the related spectra. The Sn 3d spectra of SnO<sub>2</sub>, 2% ZS, and 2% ZS/CN-15 are exhibited in Fig. 4a. The peaks at the binding energy of 486.7 eV and 495.1 eV belong to the Sn 3d<sub>5/2</sub> and Sn 3d<sub>3/2</sub> of SnO<sub>2</sub>, respectively. The 2% ZS sample displays a slight shift of the Sn 3d peak to the lower binding energy position. This change in binding energy is due to the formed oxygen vacancies by Zn doping into SnO<sub>2</sub> weakening the binding energy of the Sn<sup>4+</sup> oxidation state (Lu et al., 2018), while for 2% ZS/CN-15 composite, the binding energy peak position of Sn 3d<sub>5/2</sub> and Sn 3d<sub>3/2</sub> shift to 486.1 eV and 494.5 eV, which can be attributed to the interaction between 2% ZS and g-C<sub>3</sub>N<sub>4</sub>.

From the O 1s spectra of SnO<sub>2</sub>, 2% ZS, and 2% ZS/CN-15 samples displayed in Fig. 4b, we can observe that, compared with SnO<sub>2</sub>, the O 1s peak in 2% ZS sample is divided into two peaks, which are located at 530.1 eV and 531.3 eV, respectively, while in the 2% ZS/CN-15 sample, the O 1s peaks change to 530.9 eV and 533.2 eV, respectively. The shift of O 1s implies that there were two different kinds of chemical environments in 2% ZS and 2% ZS/CN-15 samples. Beyond that, the interaction between 2% ZS and g-C<sub>3</sub>N<sub>4</sub> in 2% ZS/CN-15 composite also could cause a shift of O 1s peaks. O 1s peaks at 530.1 eV and 530.9 eV in 2% ZS and 2% ZS/CN-15 express the coordination of oxygen originating from the Sn-O-Sn bond, while peaks at 531.3 eV and 533.2 eV denote the coordination of oxygen in Sn-O-Zn introduced by Zn doping (Ma and Wei, 2018).

The Zn 2p spectra for the 2% ZS sample can be seen in Fig. 4c. The peaks located at binding energy of 1021.9 eV and 1044.8 eV represent Zn 2p<sub>3/2</sub> and Zn 2p<sub>1/2</sub> orbital,

**Fig. 2** SEM images of g-C<sub>3</sub>N<sub>4</sub> (a), 2% ZS (b), 2% ZS/CN-15 composite (c), and EDS mappings of C (d), N (e), O (f), Sn (g), and Zn (h) of 2% ZS/CN-15 composite (c)



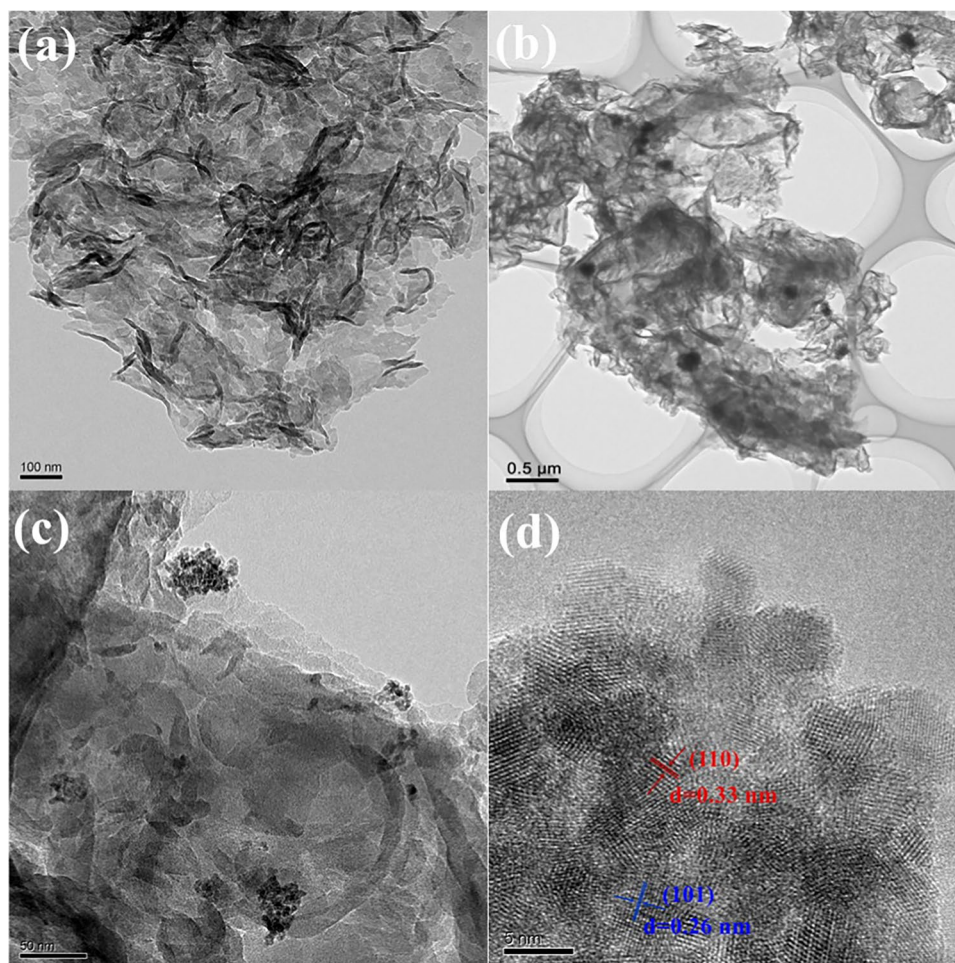
respectively, which means that Zn<sup>2+</sup> was successfully doped into SnO<sub>2</sub>.

The C 1s and N 1s spectra of 2% ZS/CN-15 are shown in Fig. 4d and Fig. 4e, respectively. The C 1s peaks located at binding energy of 284.5 eV, 286.6 eV, and 287.8 eV represent the extra carbon added to the instrument, carbon atoms in C-(N)<sub>3</sub> groups, and carbon atoms from N-C=N

in the aromatic ring structure, respectively (Zhang et al., 2021).

For N 1s spectrum, three peaks at 397.9 eV, 398.8 eV, and 402.3 eV are attributed to the nitrogen in triazine rings which contains C-N=C bond, the nitrogen atoms in N-(C)<sub>3</sub> groups, and nitrogen in -NH<sub>2</sub> groups, respectively (Zhu et al., 2021a). The results of XPS detection once again

**Fig. 3** TEM images of  $g\text{-C}_3\text{N}_4$  (a), 2% ZS/CN-15 composite (b and c), and HR-TEM image (d) of 2% ZS/CN-15 composite



proved that the materials were successfully synthesized and there was strong interaction in the 2% ZS/CN-15 composite.

### FT-IR analysis

The functional groups in the materials were tested by FT-IR technology. Fig. S1 displays the FT-IR spectra of  $\text{SnO}_2$ , 2% ZS,  $g\text{-C}_3\text{N}_4$ ,  $\text{SnO}_2/\text{CN-15}$ , and 2% ZS/CN-15 samples. For the  $\text{SnO}_2$  sample, the stretching vibration and bending vibration of the O-H bond in the hydroxyl groups of the adsorbed water can be observed at  $3416\text{ cm}^{-1}$  and  $1630\text{ cm}^{-1}$ . The peak at about  $620\text{ cm}^{-1}$  is the presentation of the Sn-O stretching vibration (Gao et al., 2018). For the 2% ZS sample, in addition to the peak that appeared at  $620\text{ cm}^{-1}$  that represents the vibration absorption of Sn-O, the slight absorption peak at  $580\text{ cm}^{-1}$  can be found as well, which belongs to the stretching vibrations of Zn-O. It is proved that  $\text{Zn}^{2+}$  was successfully doped into  $\text{SnO}_2$  material (Shanmugam et al., 2016). For  $g\text{-C}_3\text{N}_4$ , the stretching vibrations absorption of N-H bonds is reflected in peaks at  $3250\text{ cm}^{-1}$ ,  $3161\text{ cm}^{-1}$ , and  $3081\text{ cm}^{-1}$ . Peaks at  $1638\text{ cm}^{-1}$  and  $1236\text{ cm}^{-1}$  refer to the vibration absorption of C=N

and C-N bonds from the heterocyclic rings in  $g\text{-C}_3\text{N}_4$  (Paul et al., 2019b). The strong absorption peak at  $810\text{ cm}^{-1}$  is the response to the stretching vibrations of triazine units in the structure of  $g\text{-C}_3\text{N}_4$  (Wang et al., 2021c). It can be observed that  $\text{SnO}_2/\text{CN-15}$  and 2% ZS/CN-15 samples show absorption spectra similar to that of  $g\text{-C}_3\text{N}_4$ , due to the low content of  $\text{SnO}_2$  in the composites.

### Optical absorption property

The optical absorption properties of the as-prepared samples were measured employing a UV-vis spectrometer. Fig. 5a shows the spectra of  $\text{SnO}_2$ , 1–3% ZS,  $g\text{-C}_3\text{N}_4$ , and a series of 2% ZS/CN composites. The absorption curves of  $\text{SnO}_2$ -based samples and  $g\text{-C}_3\text{N}_4$ -based composite can be distinguished.  $\text{SnO}_2$  and 1–3% ZS samples show strong absorption in the ultraviolet region between 200 and 400 nm, while for  $g\text{-C}_3\text{N}_4$  and all 2% ZS/CN composites, they exhibit visible light absorption. The absorption curves of the composites are highly consistent with that of  $g\text{-C}_3\text{N}_4$ , which means that the combination with a small amount of Zn-doped  $\text{SnO}_2$  does not change the visible light absorption

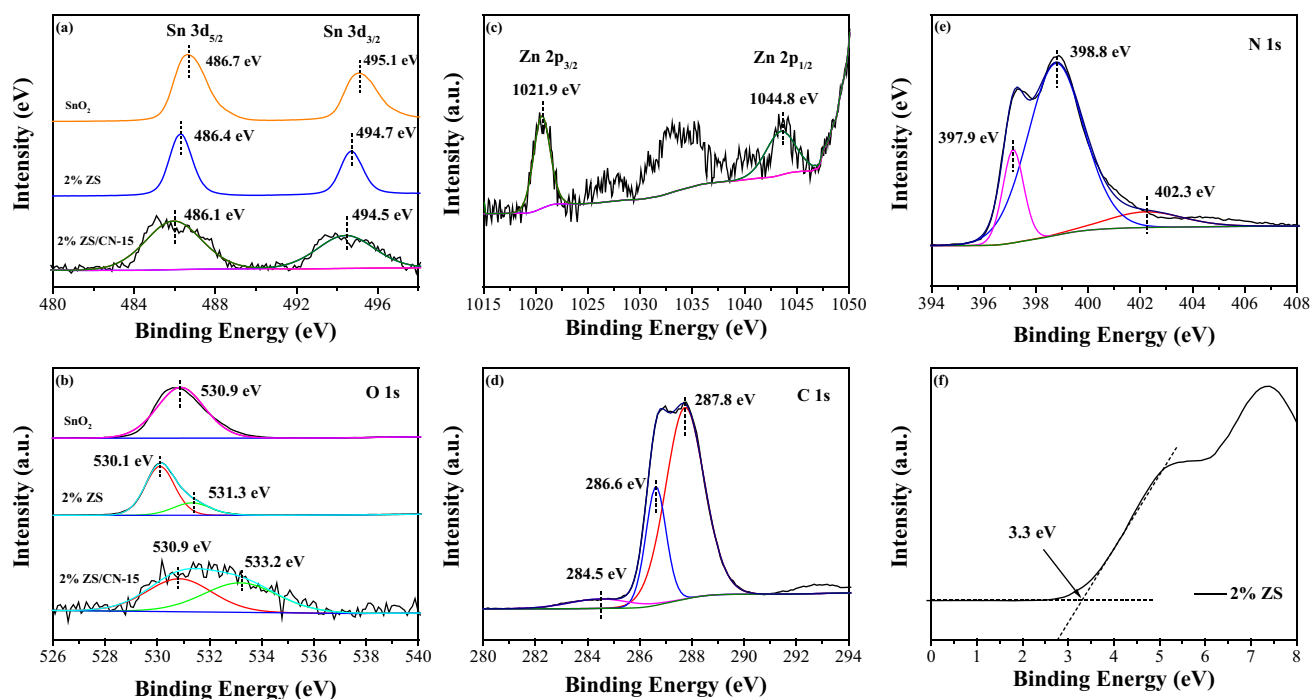


**Fig. 4** XPS spectra of Sn 3d (a) of SnO<sub>2</sub>, 2% ZS, and 2% ZS/CN-15 composite, O 1s spectra (b) of SnO<sub>2</sub>, 2% ZS, and 2% ZS/CN-15 samples, Zn 2p spectrum (c) of the 2% ZS sample, C 1s (d) and N 1s (e) spectra of 2% ZS/CN-15, and VB-XPS spectrum (f) of 2% ZS sample

capacity of g-C<sub>3</sub>N<sub>4</sub>. Also, it can be found that a slight redshift of the absorption edges occurs from Zn-doped SnO<sub>2</sub> samples. This indicates that the introduction of Zn<sup>2+</sup> expands the light absorption range of SnO<sub>2</sub>.

According to the Kubelka-Munk equation (Ji et al., 2017; Shen et al., 2017):

$$\alpha(h\nu) = A(h\nu - E_g)^{n/2} \quad (1)$$

The related curves were plotted and shown in Fig. 5b, from which the optical bandgaps of g-C<sub>3</sub>N<sub>4</sub>, SnO<sub>2</sub>, and 1–3% ZS samples were estimated. The calculated bandgaps of g-C<sub>3</sub>N<sub>4</sub> and SnO<sub>2</sub> were 2.70 eV and 3.40 eV, respectively. Besides, we can find from Fig. 5b that with the content of Zn<sup>2+</sup> gradually increasing, the bandgap of Zn-doped SnO<sub>2</sub> gradually decreases. The bandgaps of 1% ZS, 2% ZS, and 3% ZS were calculated as 3.35 eV, 3.20 eV, and 3.18 eV, respectively. The decreased band gap of ZS samples can be owing to the introduced Zn<sup>2+</sup> which occupies part of the Sn<sup>4+</sup>, and participating in the SnO<sub>2</sub> lattice network, making the formed impurity band merges into the conduction band, resulting in the narrower bandgap of the doped sample (Sol-tan et al., 2017).

### Photoluminescence (PL) analysis

The separation and recombination of photogenerated carriers are closely related to the activity of the photocatalyst. Thus,

we implemented PL experiments to explore the recombination circumstances of photogenerated electron-hole pairs in the as-synthesized photocatalysts. The PL curves were drawn based on the obtained data and shown in Fig. S2. The strongest peak centered at 460 nm can be interpreted as the fast recombination of photogenerated carriers promoting fluorescence emission in g-C<sub>3</sub>N<sub>4</sub>, while for both SnO<sub>2</sub>/CN-15 and 2% ZS/CN-15 composites, their PL signal strength is significantly lower than that of g-C<sub>3</sub>N<sub>4</sub>, which indicates that the modification of g-C<sub>3</sub>N<sub>4</sub> by SnO<sub>2</sub> could suppress the recombination of photogenerated electron-hole pairs. The PL peak intensity is the weakest for the 2% ZS/CN-15 sample, implying that the photogenerated carrier recombination rate is the lowest in this composite. The reason for this is that when Sn<sup>4+</sup> in the SnO<sub>2</sub> lattice was partly replaced by Zn<sup>2+</sup>, then the oxygen vacancy centers were formed (Wang et al., 2015) and could quickly capture photogenerated electrons of g-C<sub>3</sub>N<sub>4</sub> in the composite, thereby promoting the transfer of photogenerated electrons and inhibiting the recombination of photogenerated carriers.

### Photocatalytic activity evaluation

The application of photocatalysts to wastewater purification is of great significance to human health and safety. The degradation efficiency of pollutants depends on the photocatalytic activity of the photocatalyst. Therefore, the evaluation of the photocatalytic activities of the synthesized samples

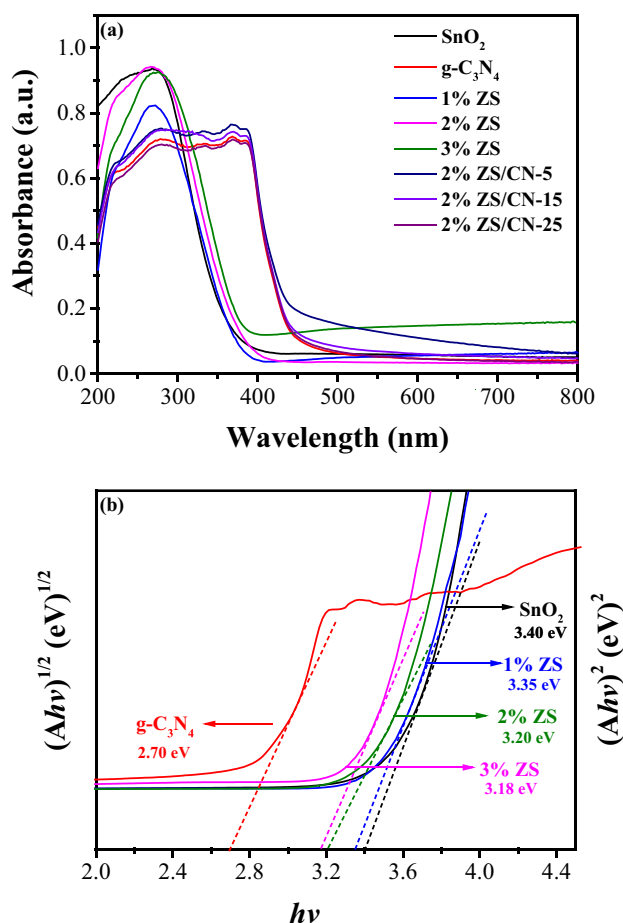


**Fig. 5** UV-vis absorption spectra (a) of SnO<sub>2</sub>, 1%–3% ZS, g-C<sub>3</sub>N<sub>4</sub>, and 2% ZS/CN composites, and the bandgap evaluation (b) of g-C<sub>3</sub>N<sub>4</sub>, SnO<sub>2</sub>, and 1%–3% ZS samples

under visible light was launched by taking the dye of RhB and the antibiotic of TC as the target contaminants. Fig. 6 shows the degradation results. As shown in Fig. 6a, 2% ZS has no degradation activity on RhB oxidation under visible light that is because it could only respond to ultraviolet light, while 54.0% RhB can be degraded in 30 min by using g-C<sub>3</sub>N<sub>4</sub>, reflecting the better visible light catalytic activity of it. We can see that the composite samples formed by doped or undoped SnO<sub>2</sub> and g-C<sub>3</sub>N<sub>4</sub> exhibit higher RhB degradation efficiency than g-C<sub>3</sub>N<sub>4</sub>. In comparison, the degradation efficiency of the composite samples combined with Zn-doped SnO<sub>2</sub> and g-C<sub>3</sub>N<sub>4</sub> is higher than that of undoped SnO<sub>2</sub>/g-C<sub>3</sub>N<sub>4</sub>. The degradation efficiencies of RhB by 1% ZS/CN-15 and 3% ZS/CN-15 samples are similar. For 2% ZS/CN samples, it can be drawn from the degradation curves that as the content of 2% ZS in the composite increases from 5 to 15%, the degradation efficiency of RhB by the composite increases, and when the content of 2% ZS continues to increase from 15 to 25%, the degradation efficiency of RhB reduced. A total of 85.6% of RhB can be degraded

within 30 min by 2% ZS/CN-15 composite, which showed the best degradation performance among the samples under visible light. And it is significantly higher than the 57.6% degradation efficiency for RhB by undoped SnO<sub>2</sub>/CN sample. For the degradation of tetracycline by the as-synthesized photocatalysts, the results are shown in Fig. 6c. Due to the poor ability to respond to visible light, 2% ZS could hardly degrade TC. Although pure g-C<sub>3</sub>N<sub>4</sub> showed the activity of degrading TC, the degradation efficiency only reached 40.3% within 90 min. When using the composite of undoped SnO<sub>2</sub> and g-C<sub>3</sub>N<sub>4</sub> (SnO<sub>2</sub>/CN-15), the degradation efficiency increased, and 56.5% TC could be degraded in 90 min. While the degradation efficiencies of TC were further improved when the composites of Zn-doped SnO<sub>2</sub> and g-C<sub>3</sub>N<sub>4</sub> were used, the degradation efficiencies of TC by using 2% ZS/CN-5, 2% ZS/CN-15 and 2% ZS/CN-25 photocatalysts were 74.6%, 86.8%, and 80.3%, respectively. When the content of ZS in the composite is the same, but the doping concentration of Zn is different, the degradation efficiency of TC is also different. The degradation efficiencies of TC by using 1% ZS/CN-15, 2% ZS/CN-15, and 3% ZS/CN-15 were 60.7%, 86.8%, and 72.3%, respectively. The composite of 2% ZS/CN-15 displayed the best photocatalytic activity for both the dye of RhB and tetracycline pollutants. Based on PL spectra and analysis, the main reason for the improvement of the photocatalytic activity can be concluded as the formation of a suitable amount of oxygen vacancies in 2% ZS and the improved photogenerated carriers' separation rate in the 2% ZS/CN-15 composite.

The photocatalytic degradation kinetics of the as-prepared photocatalysts was studied by pseudo-first-order reaction with a simplified Langmuir-Hinshelwood:

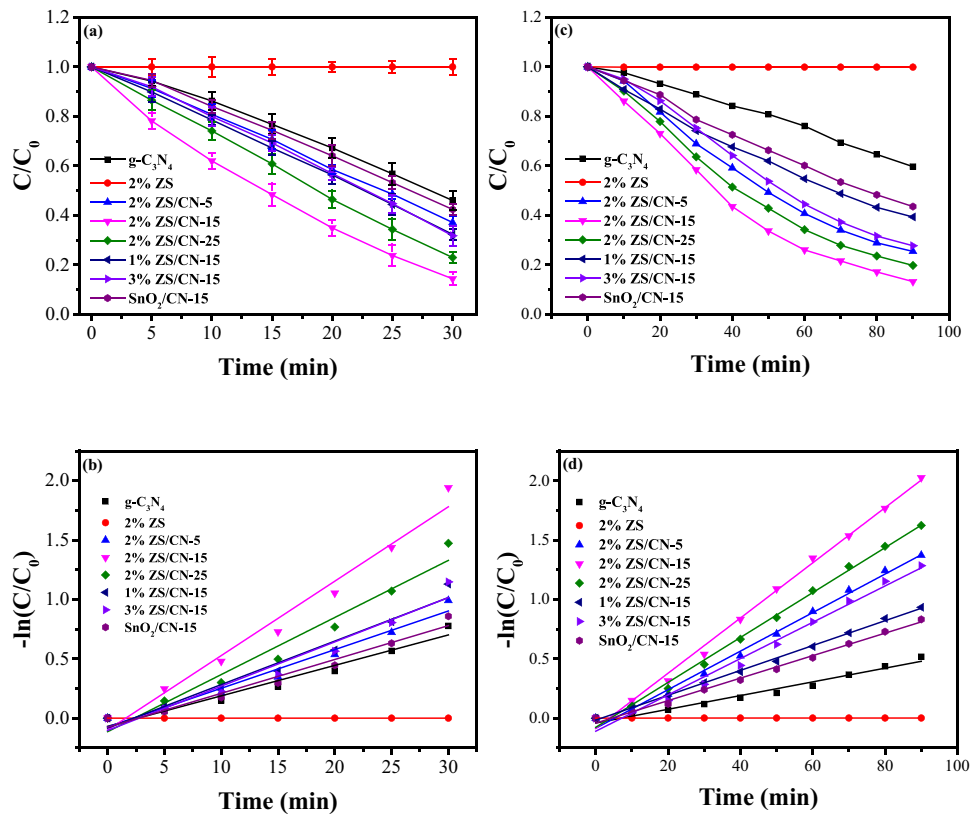
$$-\ln(C/C_0) = kt \quad (2)$$

And the corresponding rate curves were plotted and the rate constant  $k$  was calculated as well. Fig. 6b and d display the results, and from which, we can find that the  $k$  value for 2% ZS/g-C<sub>3</sub>N<sub>4</sub>-15 ( $6.27 \times 10^{-2} \text{ min}^{-1}$ ) was 2.4 times than that of g-C<sub>3</sub>N<sub>4</sub> ( $2.57 \times 10^{-2} \text{ min}^{-1}$ ) and 2.2 times than that of undoped SnO<sub>2</sub>/CN-15 samples ( $2.85 \times 10^{-2} \text{ min}^{-1}$ ) for RhB degradation. And for TC degradation, the  $k$  value for ZS/g-C<sub>3</sub>N<sub>4</sub>-15 ( $2.32 \times 10^{-2} \text{ min}^{-1}$ ) was 4.0 times than that of g-C<sub>3</sub>N<sub>4</sub> ( $5.77 \times 10^{-3} \text{ min}^{-1}$ ) and 2.4 times than that of undoped SnO<sub>2</sub>/CN-15 samples ( $9.47 \times 10^{-3} \text{ min}^{-1}$ ). We could have concluded that the degradation kinetic constant  $k$  increased with the modification of g-C<sub>3</sub>N<sub>4</sub> by Zn-doped SnO<sub>2</sub>, and when the optimal mass ratio was 15% for 2% ZS sample and g-C<sub>3</sub>N<sub>4</sub>, kinetic constant  $k$  for RhB and TC degradation reached the highest.

Then the durability performance of the prepared Zn-doped SnO<sub>2</sub>/g-C<sub>3</sub>N<sub>4</sub> composite photocatalyst was studied. And 4 cycles of degradation experiments were carried out



**Fig. 6** The degradation curves of RhB (a) and TC (c) by the as-prepared photocatalysts and the corresponding first-order kinetics fitting plots of RhB (b) and TC (d) degradation



under visible light by using the 2% ZS/CN-15 composite. The composite photocatalyst was applied to degrade RhB (or TC) until the degradation was completed. After thoroughly cleaning and drying, the composite continued to be used for the degradation of a fresh RhB (or TC) solution. And a total of 4 rounds of degradation experiments have proceeded in this way; Fig. S3a and b show the cyclic degradation results of RhB and TC. In the fourth application on RhB degradation, the 2% ZS/CN-15 composite still maintained high degradation efficiency with an RhB elimination efficiency of

81.7%. And after four consecutive degradations of TC, the degradation efficiency can still reach 82.2%. The cyclic degradation data confirms that the as-prepared low-cost composite has good recyclability. Furthermore, the photocatalytic degradation performances of RhB and TC by this work and other works were compared and summarized, which is shown in Table 1. It can be seen from Table 1 that compared to other previous works, the degradation efficiency and rate constants of RhB and TC in this work are at high levels. Therefore, it is proved that this Zn-doped SnO<sub>2</sub>/g-C<sub>3</sub>N<sub>4</sub>

**Table 1** Comparison of the degradation performance of RhB and TC between this work and other works

Photocatalysts	Light source	Target contaminant	Kinetic constant (min <sup>-1</sup> )	Degradation efficiency (%)	Reference
Nb <sub>2</sub> O <sub>5</sub> nanofibers	UV light	RhB	1.77×10 <sup>-3</sup>	59.0 (300 min)	de Jesus et al. (2021)
g-C <sub>3</sub> N <sub>4</sub> /rGO/SnO <sub>2</sub>	Visible light (halogen lamp)	RhB	2.85×10 <sup>-2</sup>	83.2 (120 min)	Ali et al. (2021)
CuO-MgO-ZnO nano-composite	Visible light (Xe lamp)	RhB	9.63×10 <sup>-3</sup>	64.3 (100 min)	Munawar et al. (2021)
TiO <sub>2</sub> /g-C <sub>3</sub> N <sub>4</sub>	Visible light (LED lamp)	TC	1.59×10 <sup>-2</sup>	79.1 (100 min)	Li et al. (2022)
L-cysteine-based g-C <sub>3</sub> N <sub>4</sub>	Visible light (LED lamp)	TC	5.90×10 <sup>-3</sup>	70.0 (180 min)	Hu et al. (2021)
g-C <sub>3</sub> N <sub>4</sub> /WO <sub>3</sub>	Simulated solar light (Xe lamp)	TC	Not mentioned	79.8 (180 min)	Jing et al. (2021)
Zn-doped SnO <sub>2</sub> /g-C <sub>3</sub> N <sub>4</sub>	Visible light (Xe lamp)	RhB	6.27×10 <sup>-2</sup>	88.6 (30 min)	This work
		TC	2.32×10 <sup>-2</sup>	86.8 (90 min)	

composite proposed in this work has a satisfactory effect on the degradation of organic pollutants, which can be regarded as a promising candidate for wastewater treatment.

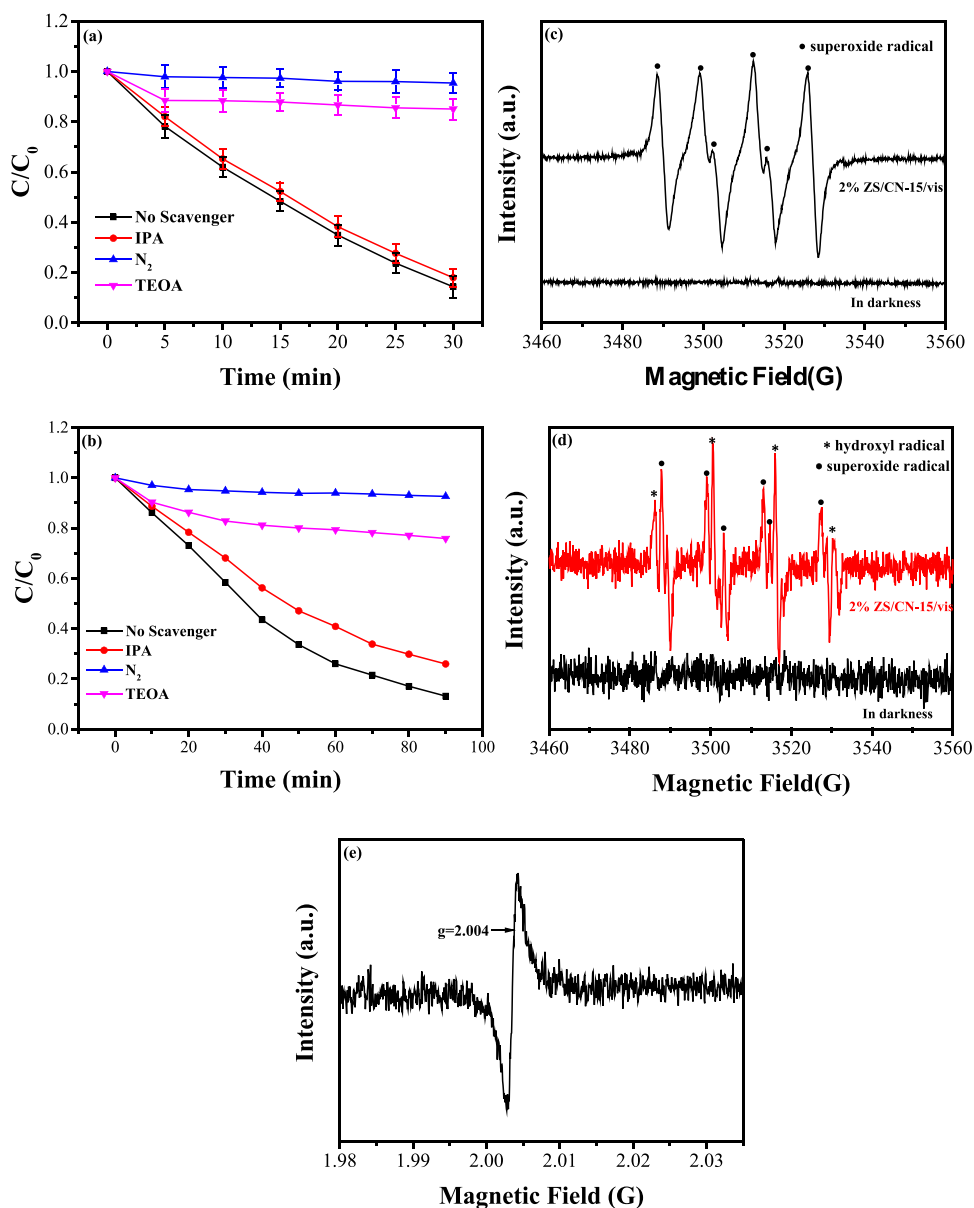
### Trapping experiments

The activity of the photocatalyst is inseparable from the active species it produces. Designing and executing the active species trapping experiments is beneficial to explore the role of the generated active species during the RhB and TC degradation process. In the process of photocatalytic reaction by using the 2% ZS/CN-15 composite, we utilized isopropanol (IPA), triethanolamine (TEOA), and nitrogen ( $N_2$ ) as the scavengers of hydroxyl radical ( $\cdot OH$ ), holes ( $h^+$ ), and superoxide radical ( $\cdot O_2^-$ ), respectively. The role

of each active species is confirmed by the consumption of the corresponding scavenger. And the results are shown in Fig. 7a and b.

For RhB degradation, the addition of IPA did not significantly inhibit the degradation, indicating that the role of hydroxyl radicals in RhB degradation is negligible. The removal efficiencies of RhB dropped to 15.0% when TEOA was added to the reaction, suggesting that  $h^+$  provided an important role in the oxidation of RhB. When  $N_2$  was brought into the photocatalytic process, the degradation efficiency of RhB was drastically reduced to 4.6%, revealing that  $\cdot O_2^-$  was the main active species produced during the photodegradation of RhB by 2% ZS/CN-15 composite photocatalyst. For the degradation of TC, when IPA was added, the degradation efficiency of TC decreased slightly, and 74.1% of TC was degraded. However, when TEOA and  $N_2$  were introduced,

**Fig. 7** The degradation curves of RhB (a) and TC (b) in the presence of 2% ZS/CN-15 composite with different scavengers, ESR spectra for superoxide radical (c), hydroxyl radical (d), and oxygen vacancy (e)



the degradation efficiency of TC was inhibited, and only 24.1% and 7.4% of TC were degraded. It shows that in the degradation of TC, the role of the scavenger is the same as in the degradation of RhB. It can be concluded that  $O_2$  is the dominant active species,  $h^+$  also plays an important role, and the effect of  $\cdot OH$  is not significant in the photocatalytic reaction carried out by the 2% ZS/CN composite photocatalyst.

ESR technology was employed to detect  $\cdot O_2^-$ ,  $\cdot OH$ , and oxygen vacancy in photocatalytic reaction over the 2% ZS/CN-15 composite sample to further verify the existence of free radicals and oxygen vacancies, and the results are displayed in Fig. 7c, Fig. 7d, and Fig. 7e, respectively. Fig. 7c shows a strong signal of  $\cdot O_2^-$ , indicating that the composite sample generated active species dominated by  $\cdot O_2^-$  under visible light irradiation, while the  $\cdot OH$  signal captured by ESR (Fig. 7d) was much weaker than that of  $\cdot O_2^-$ , and even  $\cdot O_2^-$  signals appeared in it, showing that the composite sample generated very few  $\cdot OH$  under visible light, and these  $\cdot OH$  may be formed from the reaction of  $\cdot O_2^-$  and  $H_2O$ . The results from trapping experiments and ESR tests are identical with each other, which once again illustrates the main role of  $\cdot O_2^-$  in the degradation process.

Fig. 7e shows the signals of trapped oxygen vacancy centered at  $g = 2.004$ . It demonstrates the presence of oxygen vacancies in the composite sample (Wu et al., 2021). The doped  $Zn^{2+}$  replaced a part of  $Sn^{4+}$  in the  $SnO_2$  lattice so that oxygen vacancies appeared, then the local electrons of the oxygen vacancies can be trapped to form ESR signal peaks. Active species trapping experiments and ESR detections proved that under visible light irradiation, there are a large number of  $\cdot O_2^-$ , few  $\cdot OH$ , and some oxygen vacancies existed in the photocatalytic system. That will conduce to understand the photocatalytic oxidation mechanism of RhB and TC by 2% ZS/CN composite photocatalyst.

## Photodegradation mechanism

The analysis of the bandgap structures of  $g-C_3N_4$  and 2% ZS samples can be useful for realizing the photocatalytic reaction mechanism for RhB and TC degradation by the composite photocatalyst proposed. From the previous study, we know the information that the bandgap of  $g-C_3N_4$  and 2% ZS are 2.70 and 3.20 eV, respectively. The valence band (VB) and conduction band (CB) edge potentials of  $g-C_3N_4$  were estimated according to the empirical equations (Su et al., 2021) below:

$$E_{VB} = \chi - E^0 + 0.5E_g \quad (3)$$

$$E_{CB} = E_g - E_{VB} \quad (4)$$

And by substituting the value of  $E^0 = 4.5$  and the  $\chi$  value for  $g-C_3N_4$  is 4.73 (Zhang et al., 2018), the calculated VB and CB for  $g-C_3N_4$  are 1.58 eV and  $-1.12$  eV, respectively. The  $E_{VB}$  of 2% ZS was calculated as 3.30 eV from the VB-XPS

spectrum shown in Fig. 4f. According to Equation (4), the  $E_{CB}$  of 2% ZS can be calculated as 0.1 eV.

Fig. 8 describes the possible mechanism of the photocatalytic degradation over 2% ZS/CN-15 composite based on the bandgap structures of  $g-C_3N_4$  and 2% ZS. Since  $g-C_3N_4$  could respond to visible light, when exposed to visible light, electrons on the VB of  $g-C_3N_4$  could absorb light energy and leap onto the CB of it, forming photogenerated holes and electrons. The CB position of  $g-C_3N_4$  is  $-1.12$  eV, which is more negative than the potential of  $O_2/\cdot O_2^-$  ( $-0.13$  eV vs. NHE, at pH = 7) (Zhang et al., 2020), allowing the photogenerated electrons on CB of  $g-C_3N_4$  to reduce  $O_2$  to generate  $\cdot O_2^-$ . While the VB potential of  $g-C_3N_4$  is negative than that of  $OH^-/\cdot OH$  (1.99 eV vs. NHE, at pH = 7) (Zhu et al., 2021b),  $\cdot OH$  cannot be generated via the oxidation of  $OH^-$  by holes. The  $\cdot OH$  in the photocatalytic system should be derived from the reaction of  $\cdot O_2^-$  with  $H_2O$ . For 2% ZS, according to the UV-vis absorption curve, it could only absorb ultraviolet light and cannot be excited by visible light. However, due to the doping of  $Zn^{2+}$ , oxygen vacancies were generated near the CB of the 2% ZS sample, which could capture electrons. When 2% ZS and  $g-C_3N_4$  are combined, the electrons of  $g-C_3N_4$  which is generated by the excitation of visible light migrate to the CB of the 2% ZS sample, and are captured by oxygen vacancies. This behavior can promote the separation of photogenerated carriers and inhibit the recombination of photogenerated electron-hole pairs in  $g-C_3N_4$ , thereby it further increases the generation rate of  $\cdot O_2^-$  and  $h^+$ , then the target pollutants of RhB and TC can be oxidized by  $\cdot O_2^-$  and  $h^+$ . This is why the 2% ZS/ $g-C_3N_4$  composite photocatalyst has enhanced photocatalytic activity under visible light.

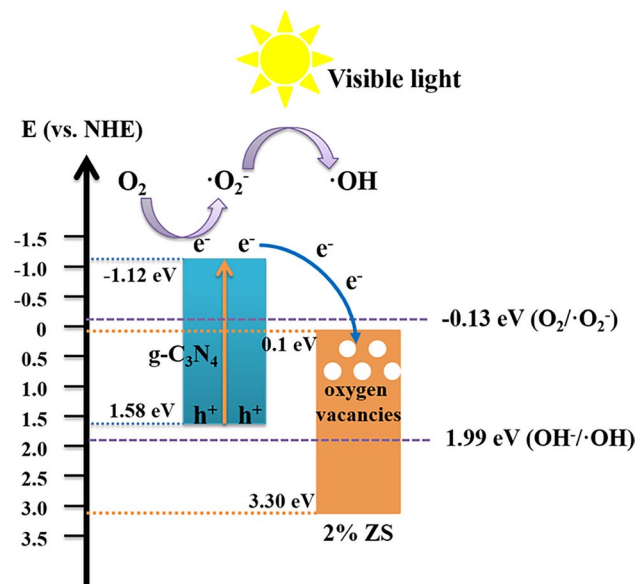


**Fig. 8** Possible degradation mechanism of 2% ZS/CN-15 composite photocatalysts under visible light

## Conclusions

We reported the synthesis of Zn-doped SnO<sub>2</sub> nanoparticles modified g-C<sub>3</sub>N<sub>4</sub> composite photocatalyst. By applying it to the degradation of organic pollutants of RhB and TC, it is found that the composite exhibited enhanced visible-light photocatalytic activity. The characterization results of XRD and SEM confirmed that Zn<sup>2+</sup> had been doped into the SnO<sub>2</sub> lattice. The chemical bond and interaction formed between g-C<sub>3</sub>N<sub>4</sub> and ZS sample are also verified by FT-IR and XPS. Active species trapping experiments showed that ·O<sub>2</sub><sup>-</sup> plays a leading role in the degradation process under visible light. Also, the results of ESR tests proved the existence of oxygen vacancies in the composite sample. In addition, the modification of g-C<sub>3</sub>N<sub>4</sub> with Zn-doped SnO<sub>2</sub> exhibited a lower photogenerated carrier recombination phenomenon than g-C<sub>3</sub>N<sub>4</sub>. This is attributed to the capture of photogenerated electrons by oxygen vacancies, which promotes the separation of photogenerated electron-hole pairs in the system. In summary, in this work, metal oxides doped with non-precious metals were used to modify g-C<sub>3</sub>N<sub>4</sub>, and the oxygen vacancies formed in the metal oxides were utilized to provide a transfer path for the photogenerated electron of g-C<sub>3</sub>N<sub>4</sub>. The formed composite photocatalyst showed enhanced performance for organics degradation. This work could provide a low-cost and high-efficiency treatment strategy for wastewater purification.

**Supplementary Information** The online version contains supplementary material available at <https://doi.org/10.1007/s11356-022-19581-5>.

**Availability of data and materials** All data generated or analyzed during this study are included in this published article.

**Author contribution** Wei Liu: writing—original draft, data curation. Qun Kang: funding acquisition, methodology. Ling Wang: investigation. Lilian Wen: investigation. Zhaohua Li: project administration. All authors read and contributed to the manuscript.

**Funding** This work was supported by the Hubei Provincial Key Research and Development Program (2020BCB067) and Research and Development of New Integrated Equipment for Rural Sewage Treatment (2021BCA129).

## Declarations

**Ethics approval and consent to participate** Not applicable.

**Consent to publish** Not applicable.

**Competing interests** The authors declare no competing interests.

## References

- Adhikari AD, Oraon R, Tiwari SK, Saren P, Maity CK, Lee JH, Hoon Kim N, Nayak GC (2018) Zn-doped SnO<sub>2</sub> nano-urchin-enriched 3D carbonaceous framework for supercapacitor application. *New J. Chem.* 42:955–963
- Ali G, Zaidi SJA, Basit MA, Park TJ (2021) Synergetic performance of systematically designed g-C<sub>3</sub>N<sub>4</sub>/rGO/SnO<sub>2</sub> nanocomposite for photodegradation of Rhodamine-B dye. *Appl. Surf. Sci.* 570:151140
- Amedlous A, Majdoub M, Amaterz E, Anfar Z, Benlhachemi A (2021) Synergistic effect of g-C<sub>3</sub>N<sub>4</sub> nanosheets/Ag<sub>3</sub>PO<sub>4</sub> microcubes as efficient n-p-type heterostructure based photoanode for photoelectrocatalytic dye degradation. *J. Photoch. Photobio. A.* 409:113127
- Balu S, Chen YL, Juang RC, Yang TC, Juan JC (2020) Morphology-controlled synthesis of alpha-Fe<sub>2</sub>O<sub>3</sub> nanocrystals impregnated on g-C<sub>3</sub>N<sub>4</sub>-SO<sub>3</sub>H with ultrafast charge separation for photoreduction of Cr (VI) under visible light. *Environ. Pollut.* 267:115491
- Chen Z, Zhang S, Liu Y, Alharbi NS, Rabah SO, Wang S, Wang X (2020) Synthesis and fabrication of g-C<sub>3</sub>N<sub>4</sub>-based materials and their application in elimination of pollutants. *Sci. Total. Environ.* 731:139054
- Chu YC, Lin TJ, Lin YR, Chiu WL, Nguyen BS, Hu C (2020) Influence of P, S, O-Doping on g-C<sub>3</sub>N<sub>4</sub> for hydrogel formation and photocatalysis: An experimental and theoretical study. *Carbon.* 169:338–348
- Jesus ETD, Moreira AJ, Sá MC, Freschi GPG, Joya MR, Li MS, Paris EC (2021) Potential of Nb<sub>2</sub>O<sub>5</sub> nanofibers in photocatalytic degradation of organic pollutants. *Environ. Sci. Pollut. R.* 28:69401–69415
- Ding H, Han D, Han Y, Liang Y, Liu X, Li Z, Zhu S, Wu S (2020) Visible light responsive CuS/protonated g-C<sub>3</sub>N<sub>4</sub> heterostructure for rapid sterilization. *J. Hazard. Mater.* 393:122423
- Feng C, Tang L, Deng Y, Wang J, Liu Y, Ouyang X, Yang H, Yu J, Wang J (2021) A novel sulfur-assisted annealing method of g-C<sub>3</sub>N<sub>4</sub> nanosheet compensates for the loss of light absorption with further promoted charge transfer for photocatalytic production of H<sub>2</sub> and H<sub>2</sub>O<sub>2</sub>. *Appl. Catal. B Environ.* 281:119539
- Gao WY, Zhao Y, Mao Z, Bi D, Chen J, Wang D (2018) Enhanced visible light photocatalytic activity for g-C<sub>3</sub>N<sub>4</sub>/SnO<sub>2</sub>: Sb composites induced by Sb doping. *J. Mater. Sci.* 53:9473–9485
- Guo H, Wan S, Wang Y, Ma W, Zhong Q, Ding J (2021) Enhanced photocatalytic CO<sub>2</sub> reduction over direct Z-scheme NiTiO<sub>3</sub>/g-C<sub>3</sub>N<sub>4</sub> nanocomposite promoted by efficient interfacial charge transfer. *Chem. Eng. J.* 412:128646
- Hu C, Liu ZT, Yang PC, Ding YX, Lin KYA, Nguyen BS (2021) Self-assembly L-cysteine based 2D g-C<sub>3</sub>N<sub>4</sub> nanoflakes for light-dependent degradation of rhodamine B and tetracycline through photocatalysis. *J. Taiwan Inst. Chem. E.* 123:219–227
- Huang S, Ali N, Huai Z, Ren J, Sun Y, Zhao X, Fu G, Kong W, Yang S (2020) A facile strategy for enhanced performance of inverted organic solar cells based on low-temperature solution-processed SnO<sub>2</sub> electron transport layer. *Org. Electron.* 78:105555
- Ismael M (2020) A review on graphitic carbon nitride (g-C<sub>3</sub>N<sub>4</sub>) based nanocomposites: synthesis, categories, and their application in photocatalysis. *J. Alloy. Compd.* 846:156446
- Ji HY, Fan Y, Yan J, Xu Y, She X, Gu J, Fei T, Xu H, Li H (2017) Construction of SnO<sub>2</sub>/graphene-like g-C<sub>3</sub>N<sub>4</sub> with enhanced visible light photocatalytic activity. *RSC Adv.* 7:36101–36111
- Jing H, Ou R, Yu H, Zhao Y, Lu Y, Huo M, Huo H, Wang X (2021) Engineering of g-C<sub>3</sub>N<sub>4</sub> nanoparticles/WO<sub>3</sub> hollow microspheres photocatalyst with Z-scheme heterostructure for boosting tetracycline hydrochloride degradation. *Sep. Purif. Technol.* 255:117646
- Li Y, Ti M, Zhao D, Zhang Y, Wu L, He Y (2021) Facile synthesis of nitrogen-vacancy pothole-rich few-layer g-C<sub>3</sub>N<sub>4</sub> for photocatalytic nitrogen fixation into nitrate and ammonia. *J. Alloy. Compd.* 870:159298
- Li Y, Zhang Q, Lu Y, Song Z, Wang C, Li D, Tang X, Zhou X (2022) Surface hydroxylation of TiO<sub>2</sub>/g-C<sub>3</sub>N<sub>4</sub> photocatalyst for photo-Fenton degradation of tetracycline. *Ceram. Int.* 48:1306–1313

- Li Y, Zhou M, Cheng B, Shao Y (2020) Recent advances in g-C<sub>3</sub>N<sub>4</sub>-based heterojunction photocatalysts. *J. Mater. Sci. Technol.* 56:1–17
- Liu G, Huang Y, Lv H, Wang H, Zeng Y, Yuan M, Meng Q, Wang C (2021a) Confining single-atom Pd on g-C<sub>3</sub>N<sub>4</sub> with carbon vacancies towards enhanced photocatalytic NO conversion. *Appl. Catal. B Environ.* 284:119683
- Liu J, Zhang Q, Tian X, Hong Y, Nie Y, Su N, Jin G, Zhai Z, Fu C (2021b) Highly efficient photocatalytic degradation of oil pollutants by oxygen deficient SnO<sub>2</sub> quantum dots for water remediation. *Chem. Eng. J.* 404:127146
- Liu W, Li Z, Kang Q, Wen L (2021c) Efficient photocatalytic degradation of doxycycline by coupling  $\alpha$ -Bi<sub>2</sub>O<sub>3</sub>/g-C<sub>3</sub>N<sub>4</sub> composite and H<sub>2</sub>O<sub>2</sub> under visible light. *Environ. Res.* 197:110925
- Liu W, Zhou J, Zhou Y, Liu D (2021) Peroxymonosulfate-assisted g-C<sub>3</sub>N<sub>4</sub>@Bi<sub>2</sub>MoO<sub>6</sub> photocatalytic system for degradation of nimesulide through phenyl ether bond cleavage under visible light irradiation. *Sep. Purif. Technol.* 264:118288
- Lu C, Wang J, Xu F, Wang A, Meng D (2018) Zn-doped SnO<sub>2</sub> hierarchical structures formed by a hydrothermal route with remarkably enhanced photocatalytic performance. *Ceram. Int.* 44:15145–15152
- Ma LA, Wei ZH (2018) Effect of synthesis conditions on the morphology and field-emission properties of hydrothermally grown Zn-doped SnO<sub>2</sub> nanorods. *CrystEngComm.* 20:1422–1430
- Matussin SN, Harunsani MH, Tan AL, Cho MH, Khan MM (2020) Effect of Co<sup>2+</sup> and Ni<sup>2+</sup> co-doping on SnO<sub>2</sub> synthesized via phyto-genic method for photoantioxidant studies and photoconversion of 4-nitrophenol. *Mater. Today Commun.* 25:101677
- Munawar T, Mukhtar F, Yasmeen S, Naveed-Ur-Rehman M, Nadeem MS, Riaz M, Mansoor M, Iqbal F (2021) Sunlight-induced photocatalytic degradation of various dyes and bacterial inactivation using CuO-MgO-ZnO nanocomposite. *Environ. Sci. Pollut. R.* 28:42243–42260
- Pacheco-Salazar DG, Aragón FFH, Villegas-Lelovsky L, Ortiz de Zevallos A, Marques GE, Coaquira JAH (2020) Engineering of the band gap induced by Ce surface enrichment in Ce-doped SnO<sub>2</sub> nanocrystals. *Appl. Surf. Sci.* 527:146794
- Paul DR, Gautam S, Panchal P, Nehra SP, Choudhary P, Sharma A (2020a) ZnO-Modified g-C<sub>3</sub>N<sub>4</sub>: a potential photocatalyst for environmental application. *ACS Omega.* 5:3828–3838
- Paul DR, Sharma R, Nehra SP, Sharma A (2019a) Effect of calcination temperature, pH and catalyst loading on photodegradation efficiency of urea derived graphitic carbon nitride towards methylene blue dye solution. *RSC Adv.* 9:15381–15391
- Paul DR, Sharma R, Panchal P, Malik R, Sharma A, Tomer VK, Nehra SP (2019b) Silver doped graphitic carbon nitride for the enhanced photocatalytic activity towards organic dyes. *J. Nanosci. Nanotechnol.* 19:5241–5248
- Paul DR, Sharma R, Panchal P, Nehra SP, Gupta AP, Sharma A (2020b) Synthesis, characterization and application of silver doped graphitic carbon nitride as photocatalyst towards visible light photocatalytic hydrogen evolution. *Int. J. Hydrogen Energ.* 45:23937–23946
- Paul DR, Nehra SP (2021) Graphitic carbon nitride: a sustainable photocatalyst for organic pollutant degradation and antibacterial applications. *Environ. Sci. Pollut. R.* 28:3888–3896
- Phuoc PH, Hung CM, Van Toan N, Van Duy N, Hoa ND, Van Hieu N (2020) One-step fabrication of SnO<sub>2</sub> porous nanofiber gas sensors for sub-ppm H<sub>2</sub>S detection. *Sensor. Actuat. A Phys.* 303:111722
- Shanmugam N, Sathya T, Viruthagiri G, Kalyanasundaram C, Gobi R, Ragupathy S (2016) Photocatalytic degradation of brilliant green using undoped and Zn doped SnO<sub>2</sub> nanoparticles under sunlight irradiation. *Appl. Surf. Sci.* 360:283–290
- Shen H, Zhao X, Duan L, Liu R, Li H (2017) Enhanced visible light photocatalytic activity in SnO<sub>2</sub>@g-C<sub>3</sub>N<sub>4</sub> core-shell structures. *Mat. Sci. Eng. B.* 218:23–30
- Sivakumar P, Akkera HS, Ranjeth Kumar Reddy T, Srinivas Reddy G, Kambhala N, Nanda Kumar Reddy N (2021) Influence of Ga doping on structural, optical and electrical properties of transparent conducting SnO<sub>2</sub> thin films. *Optik.* 226:165859
- Soltan WB, Ammar S, Olivier C, Toupance T (2017) Influence of zinc doping on the photocatalytic activity of nanocrystalline SnO<sub>2</sub> particles synthesized by the polyol method for enhanced degradation of organic dyes. *J. Alloy. Compd.* 729:638–647
- Song YF, Liu JM, Ge F, Huang X, Zhang Y, Ge HH, Meng XJ, Zhao YZ (2021) Influence of Nd-doping on the degradation performance of Ti/Sb-SnO<sub>2</sub> electrode. *J. Environ. Chem. Eng.* 9:105409
- Su X, Chen W, Han Y, Wang D, Yao J (2021) In-situ synthesis of Cu<sub>2</sub>O on cotton fibers with antibacterial properties and reusable photocatalytic degradation of dyes. *Appl. Surf. Sci.* 536:147945
- Sun Q, Hu X, Zheng S, Zhang J, Sheng J (2019) Effect of calcination on structure and photocatalytic property of N-TiO<sub>2</sub>/g-C<sub>3</sub>N<sub>4</sub>@diatomite hybrid photocatalyst for improving reduction of Cr(VI). *Environ. Pollut.* 245:53–62
- Sun S, Li C, Sun Z, Wang J, Wang X, Ding H (2021) In-situ design of efficient hydroxylated SiO<sub>2</sub>/g-C<sub>3</sub>N<sub>4</sub> composite photocatalyst: synergistic effect of compounding and surface hydroxylation. *Chem. Eng. J.* 416:129107
- Wang J, Fan H, Yu H (2015) Synthesis of hierarchical porous Zn-Doped SnO<sub>2</sub> spheres and their photocatalytic properties. *J. Mater. Eng. Perform.* 24:4260–4266
- Wang W, Niu Q, Zeng G, Zhang C, Huang D, Shao B, Zhou C, Yang Y, Liu Y, Guo H, Xiong W, Lei L, Liu S, Yi H, Chen S, Tang X (2020) 1D porous tubular g-C<sub>3</sub>N<sub>4</sub> capture black phosphorus quantum dots as 1D/0D metal-free photocatalysts for oxytetracycline hydrochloride degradation and hexavalent chromium reduction. *Appl. Catal. B Environ.* 273:119051
- Wang W, Tao Y, Du L, Wei Z, Yan Z, Chan WK, Lian Z, Zhu R, Phillips DL, Li G (2021a) Femtosecond time-resolved spectroscopic observation of long-lived charge separation in bimetallic sulfide/g-C<sub>3</sub>N<sub>4</sub> for boosting photocatalytic H<sub>2</sub> evolution. *Appl. Catal. B Environ.* 282:119568
- Wang Y, Huang H, Zhang Z, Wang C, Yang Y, Li Q, Xu D (2021c) Lead-free perovskite Cs<sub>2</sub>AgBiBr<sub>6</sub>@g-C<sub>3</sub>N<sub>4</sub> Z-scheme system for improving CH<sub>4</sub> production in photocatalytic CO<sub>2</sub> reduction. *Appl. Catal. B Environ.* 282:119570
- Wu H, Wang J, Chen R, Yuan C, Zhang J, Zhang Y, Sheng J, Dong F (2021) Zn-doping mediated formation of oxygen vacancies in SnO<sub>2</sub> with unique electronic structure for efficient and stable photocatalytic toluene degradation. *Chinese J. Catal.* 42:1195–1204
- Xue S, Wu C, Pu S, Hou Y, Tong T, Yang G, Qin Z, Wang Z, Bao J (2019) Direct Z-Scheme charge transfer in heterostructured MoO<sub>3</sub>/g-C<sub>3</sub>N<sub>4</sub> photocatalysts and the generation of active radicals in photocatalytic dye degradations. *Environ. Pollut.* 250:338–345
- Yakout SM (2021) Robust ferromagnetic and fast sunlight photocatalytic properties of nanocrystalline SnO<sub>2</sub>: Co/Cu codoping. *Ceram. Int.* 47:10104–10112
- Zhang J, Xin B, Shan C, Zhang W, Dionysiou DD, Pan B (2021) Roles of oxygen-containing functional groups of O-doped g-C<sub>3</sub>N<sub>4</sub> in catalytic ozonation: quantitative relationship and first-principles investigation. *Appl. Catal. B Environ.* 292:120155
- Zhang L, Wang G, Xiong Z, Tang H, Jiang C (2018) Fabrication of flower-like direct Z-scheme  $\beta$ -Bi<sub>2</sub>O<sub>3</sub>/g-C<sub>3</sub>N<sub>4</sub> photocatalyst with enhanced visible light photoactivity for Rhodamine B degradation. *Appl. Surf. Sci.* 436:162–171
- Zhang T, Wang X, Sun Z, Liang Q, Zhou M, Xu S, Li Z, Sun D (2020) Constructing Z-scheme based BiOI/CdS heterojunction with

- efficient visible-light photocatalytic dye degradation. *Solid State Sci.* 107:106350
- Zhao QQ, Deng X, Ding M, Gan L, Zhai T, Xu X (2015) One-pot synthesis of Zn-doped SnO<sub>2</sub> nanosheet-based hierarchical architectures as a glycol gas sensor and photocatalyst. *CrystEngComm.* 17:4394–4401
- Zhu X, Wang Y, Guo Y, Wan J, Yan Y, Zhou Y, Sun C (2021a) Environmental-friendly synthesis of heterojunction photocatalysts g-C<sub>3</sub>N<sub>4</sub>/BiPO<sub>4</sub> with enhanced photocatalytic performance. *Appl. Surf. Sci.* 544:148872
- Zhu Y, Cui Y, Xiao B, Ou-yang J, Li H, Chen Z (2021b) Z-scheme 2D/2D g-C<sub>3</sub>N<sub>4</sub>/Sn<sub>3</sub>O<sub>4</sub> heterojunction for enhanced visible-light photocatalytic H<sub>2</sub> evolution and degradation of ciprofloxacin. *Mat. Sci. Semicon. Proc.* 129:105767

**Publisher's note** Springer Nature remains neutral with regard to jurisdictional claims in published maps and institutional affiliations.